Role of Austenitization Temperature on Structure Homogeneity and Transformation Kinetics in Austempered Ductile Iron

M. Górny[1] · G. Angella[2] · E. Tyrała[1] · M. Kawalec[1] · S. Paź[1] · A. Kmita[3]

Abstract

This paper considers the important factors of the production of high-strength ADI (Austempered Ductile Iron); namely, the austenitization stage during heat treatment. The two series of ADI with different initial microstructures were taken into consideration in this work. Experiments were carried out for castings with a 25-mm-walled thickness. Variable techniques (OM, SEM, dilatometry, DSC, Variable Magnetic Field, hardness, and impact strength measurements) were used for investigations of the influence of austenitization time on austempering transformation kinetics and structure in austempered ductile iron. The outcome of this work indicates that the austenitizing temperature has a very significant impact on structure homogeneity and the resultant mechanical properties. It has been shown that the homogeneity of the metallic matrix of the ADI microstructure strongly depends on the austenitizing temperature and the initial microstructure of the spheroidal cast irons (mainly through the number of graphite nodules). In addition, this work shows the role of the austenitization temperature on the formation of Mg–Cu precipitations in ADI.

Keywords Metals · Casting · ADI · Heat treatment · Mg_2Cu particles

1 Introduction

Austempered ductile iron (ADI) belongs to the spheroidal graphite cast iron (SGI) family, which is subjected to heat treatment; i.e., austenitization and austempering. As a result of this heat treatment, a rather advantageous combination of strength, ductility, and toughness is obtained [1–4]. This in turn allows ADI to be an alloy that is competitive with steel and aluminum alloys in terms of its mechanical properties, production cost, and weight saving. From the viewpoint of material selection, ADI is therefore the most cost-effective solution in many applications, including automotive and

light/heavy trucks, construction and mining equipment, railroad, agricultural, gears and crankshafts, and brackets, among others [5–7]. In the literature, numerous papers have been published on ADI: particularly, on the numerical simulation [8–10], kinetics of austenitizing and austempering processes [3–8], effect of alloying elements [11–14], structure formation [15–17], mechanical and fatigue properties [18–22], machinability [23], and other applications [24].

The structure of ADI cast iron consists of spheroidal graphite nodules imbedded in a metallic matrix of plates of ferrite and high-carbon austenite. The shaping of the ADI structure depends on factors related to the SGI production process (mainly, the chemical composition and spheroidization as well as inoculation treatments) and the heat treatment parameters (which are austenitization and austempering). During the austempering stage, the austenite decomposes into ferrite plates and high-carbon austenite, and the final ADI structure formation takes place [6]. The number of graphite nodules, their shapes and distribution, the number and morphology of the ferrite plates, and the high-carbon austenite determine the final properties of ADI cast iron.

However, the austenitizing process that is the first step of heat treatment is also of significant importance in designing and shaping the structure of ADI. The austenitizing stage

✉ M. Górny
   mgorny@agh.edu.pl

1   Faculty of Foundry Engineering, Department of Cast Alloys and Composites Engineering, AGH University of Science and Technology, Reymonta St. 23, 30-059 Kraków, Poland

2   Institute of Condensed Matter Chemistry and Technologies for Energy (ICMATE), National Research Council of Italy (CNR), Via R. Cozzi 53, 20125 Milan, MI, Italy

3   Academic Centre for Materials and Nanotechnology, AGH University of Science and Technology, al. Mickiewicza 30, 30-059 Kraków, Poland

has been studied by many researchers. Darwish and Elliott [12–14] studied the effect of austenitizing temperature and time on the carbon content in austenite that increases with increasing temperatures. Also, the holding time affects the carbon saturation in austenite, but this increase takes place most extensively at the initial stage of austenitizing. From [25], it follows that a higher austenitizing temperature increases the austenite fraction in the microstructure. Moreover, it delays the austempering reaction [26] and decreases the thermodynamic driving force for the austempering reaction, generating fewer ferrite nuclei, resulting in a coarser ADI structure [12–14, 25]. The research [12] also shows that raising the austenitizing temperature does not favor the formation of a homogeneous structure. Moore [27] stated that the martensite fraction in the ADI cast iron metallic matrix also depends on the austenitizing temperature and alloying elements. The high austenitizing temperature contributes to the increased risk of martensite occurrence. Finally, Keough [24] reported that hardenability increases while the mechanical properties decrease with increasing austenitizing temperatures. During the austenitizing process, a Mg–Cu reaction also occurs, which results in the creation of highly dispersive Mg_2Cu precipitations [28]. The Mg_2Cu particles grow in the copper-magnesium-saturated regions near the graphite nodules, which can introduce microcracks in ADI castings. The existence of these microcracks in castings should be also taken into account in optimizing the structure and mechanical properties of ADI (as reported in [28]).

So, the production route to design and shape optimal ADI structures with proper mechanical properties is complex, involving melt treatment, modification, inoculation and the subsequent heat treatments of the austempering process. The present research aims to enrich the knowledge of the significant impact of the melt treatment to have different initial graphite structures and the first heat treatment period (i.e., austenitization) on the austempering process kinetics, structural homogeneity, and properties of ADI cast irons as well as on the formation of highly disperse precipitations from the Mg–Cu system.

2 Experimental Procedures

The experimental melts were prepared in a 15-kg-capacity crucible using an electrical induction furnace of intermediate frequency. The furnace charge consisted of Sorel-metal (High-Purity Pig Iron: 4.46% C, 0.132% Si, 0.01% Mn, 0.006% S, 0.02% P), technically pure silica, Fe–Mn, steel scrap, copper, and nickel. After melting at 1490 °C, the liquid metal was held for 2 min followed by spheroidization and inoculation operations using a bell method. An Fe–Si–Mg (6% Mg) foundry alloy was used for spheroidization, while Foundrysil (73–78% Si, 0.75–1.25% Ca,

0.75–1.25% Ba, 0.75–1.25% Al, Fe [balance]) was used for inoculation purposes. The cast iron was poured at 1400 °C into Y block ingots (25 mm) following the ASTM A 536-84 standard. The two series (Alloys A and B) of melts were carried out to attain different nucleation potentials of the graphite and, ultimately, different numbers of the graphite nodule counts. Different nucleation potential of graphite was attained by holding times of the liquid metal after spheroidization and inoculation treatment (i.e., metal treatment). Alloy B was casted 1 min (super-inoculated state) whereas Alloy A was casted after 5 min after metal treatment.

The chemical composition tests of the experimental ductile irons were carried out using a SPECTRAMAXx emission spectrometer with spark excitation. To determine the kinetics of the austempering process, the dilatometric studies were performed using a DI-105 absolute dilatometer. The temperature of the austenitic transformation (Ac1) was determined by dilatometric studies and using DSC differential scanning calorimetry using a TA Instruments SDT Q600 thermo-gravimeter. The implemented heat treatments for ADI production consisted of the following: (a) austenitizing in a silite furnace at temperatures of 860 °C, 880 °C, 900 °C, and 920 °C for 2 h; (b) austempering in a salt bath of $NaNO_2$–KNO_3 at 380 °C for 2 h; and (c) air cooling to room temperature.

In addition, a JEOL JSM-5500LV scanning electron microscope (SEM) and optical microscope (OM) Leica MEF4M equipped with quantitative analyzer Leica QWin v3.5 were used for the metallographic characterization of the graphite (graphite fraction, number of graphite nodules, mean free distance between graphite nodules, and mean diameter of graphite nodules) and metallic matrix.

The volume fraction of the austenite was determined by means of a variable magnetic field (VMF). It was assumed that, in the reversible range of the magnetic field, the magnetic dispersion of the alloy (k_s) can be determined by Eq. (1) [29]:

$$k_s = \sum k_{\alpha i} \cdot V_{\alpha i} \tag{1}$$

where k_s–magnetic dispersion of alloy; $k_{\alpha i}$–magnetic dispersion of i-th phase component; $V_{\alpha i}$–volumetric fraction of i-th phase.

For ADI cast iron with a specific magnetic dispersion value of k_s, the volume fraction of austenite V_γ can be expressed as follows:

$$V_\gamma = (k_s - k_{F-G})/(k_A - k_{F-G}) \cdot 100 [\%] \tag{2}$$

where $k_{F-G} = 0.120$—magnetic dispersion specified for spheroidal graphite cast iron with ferritic matrix (after ferrite annealing); $k_A = 0.775$—austenite magnetic dispersion [29].

Alloy	C	Si	Mn	P	S	Mg	Cu	Ni
Chemical composition (wt%)								
A	3.40	2.25	0.25	0.01	0.01	0.05	1.05	1.40
B	3.41	2.15	0.09	0.037	0.01	0.05	0.98	1.40

Table 1 Chemical composition of the investigated ADI samples
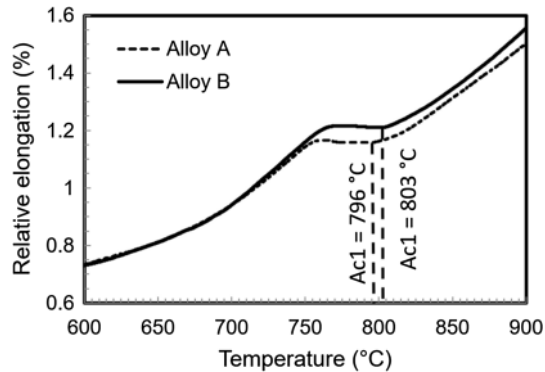
Fig. 1 Dilatometry curves for Alloys A and B

Fig. 2 DSC curves for Alloys A and B

In addition, Brinell hardness measurements were made using an HPO-250 hardness tester, while an unnotched Charpy test was performed on $55 \times 10 \times 10$ mm specimens complying to the A327-80 ASTM specification; these specimens were machined from the bottom part of these Y-shaped castings.

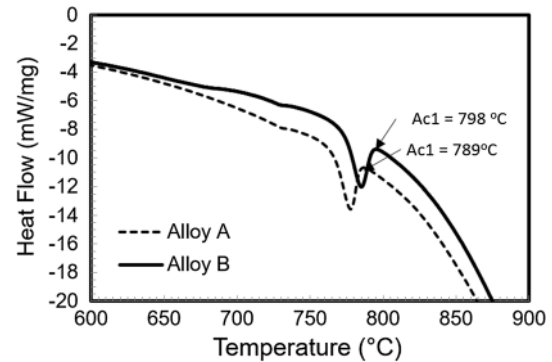## 3 Results and discussion

3.1 Chemical composition and temperature of austenitic transformation (Ac1)

The results of the chemical composition tests of the experimental ADI samples are shown in Table 1.

Both of the analyzed alloys (A and B) contained copper and nickel, which are usually used in ADI cast iron to obtain a pearlitic matrix of the base iron and increase the hardenability during the austempering process. From the point of view of the chemical composition, the tested ADI cast iron in Alloys A and B possessed differences that, above all, referred to the content of Mn, which is a carbide-forming element and segregates to the boundaries of the eutectic grains.

Figure 1 shows the dilatometric curves from the heating samples to determine the temperature of the austenitic transformation.

The temperature of the end of the pearlite-to-austenite transformation is 796 °C and 803 °C for Alloys A and B, respectively. The dilatometry results were confirmed by a DSC study (Fig. 2). The DSC curves show that the

temperatures at which the austenitic transformation (Ac1) takes place in Samples A and B are 789 °C and 798 °C, respectively.

The reduced temperature for Alloy A is the result of a higher content of Mn in the ductile iron (see Table 1). The equilibrium austenitizing temperature estimated by the two methods differs slightly. The deviation does not exceed 7 °C. Usually, in the production of ADI cast iron, the austenitization temperature is set to 900 °C [6]. During austenitizing, the graphite continuously provides carbon for the austenite; therefore, the diffusion rate of the carbon in the austenite (for a given austenitizing temperature) depends on the graphite fraction and distances between the graphite nodules. The higher the number of graphite nodules, the faster the carbon diffusion will be due to the shorter carbon diffusion paths. Increases in austenitizing temperature (T_γ) causes the carbon content in the austenite to increase according to Formula [12]:

$$C_\gamma^\circ = T_\gamma/420 - 0.17(\%Si) - 0.95 \qquad (3)$$

Due to the presence of carbon and other elements like Si, Mn, Cu, Mo, or Ni in the ductile iron, the phase transformation of the austenite is controlled by the diffusion of these elements.

It is also worth mentioning that the content of carbon and other elements in austenite has a significant influence on the process of the nucleation and growth of the ferrite plates during the subsequent austempering process. A higher austenitizing temperature will lead to a higher carbon concentration in the austenite, which will result in a lower number of ferrite plates. This is consistent with Rao's studies [25]. Following

Rundman [26] the schematic of T–C section in the Fe–C phase diagram is shown in Fig. 3. Increasing the austenitizing temperature decreases the driving forces expressed here as Δw_c for the austempering reaction: $\Delta w_{c4} > \Delta w_{c3} > \Delta w_{c2} > \Delta w_{c1}$ (Fig. 3) and increases the austempering time needed to obtain high-carbon austenite. This will result in a more inhomogeneous structure.

The ferrite plate nucleation process affects the fraction and morphology of high-carbon austenite as well as the homogeneity of the metallic matrix. A lower number of ferrite plates will lead to a greater heterogeneity of the metallic matrix by creating a higher fraction of the blocky type of high-carbon austenite as well as the greater thermodynamic instability of the austenite (which can undergo partial transformation into martensite).

3.2 Kinetics of austempering transformation

The kinetics of the austempering transformation was followed by dilatometric means. The relative expansion of the ductile iron as a function of time and temperature was carried out. Exponential Eq. (4) was used to characterize the isothermal transformation processes during austempering:
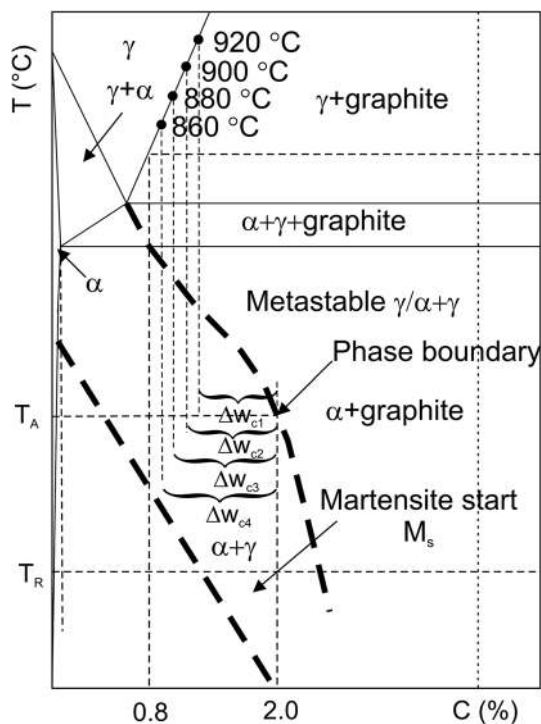
$$f = \exp(-1/n \cdot t) \tag{4}$$

Fig. 3 A schematic Temperature-Carbon concentration section in the Fe–C phase diagram. Driving force for austempering transformation: $\Delta w_{c4} > \Delta w_{c3} > \Delta w_{c2} > \Delta w_{c1}$. Adapted from Ref. [26]

where f is the volume fraction of the transformation product, and n is a curve-shape constant valid for a given transformation condition. Figure 4a, b show dilatometric curves that indicate the degree of transformation (f) as a function of the austempering time (t) in the investigated A and B alloys.

Figure 4c, d show the first derivatives of the dilatometric curves with respect to time (indicating the transformation rates). From these results, the quantitative parameters describing the austempering transformation kinetics were determined; these are provided in Table 2.

The data summarized in Table 2 show that the incubation time for Alloys A and B is more or less the same for a given temperature of austenitizing. In turn, the austenitizing temperature has a significant effect on the incubation time. Raising the austenitizing temperature increases the incubation time. An increase in the incubation time is associated with an increase in the carbon content in the austenite after the austenitizing process. The austenitizing temperature also has a significant effect on the transformation rate [maximums on the kinetic curves (Fig. 4c, d)]. Raising the austenitizing temperature reduces this transformation rate. In other words, both the increase of incubation times and reduction of kinetics rates with higher austenitization temperatures can be rationalized by the decrease of the driving force of austempering with increasing austenitization temperatures in agreement with the scheme in Fig. 3. This transformation rate strongly depends on the initial microstructure (the number of graphite nodules, their diameter, and the distance between them) that affect the kinetics, through affecting ultimately the number of the nuclei of the ferrite plates formed at the beginning of the austempering transformation. A greater number of ferrite nuclei are formed with a greater number of graphite nodules (refined microstructure). The maximums on the kinetic curves are identified with the maximum nucleation and growth rate of the ferrite plates. The austenitizing temperature also has a significant effect on the total transformation time; after this, the microstructure of the ausferrite (irregular ferrite plates and stable high-carbon austenite) is achieved.

3.3 Microstructure

Figures 5 and 6 show micrographs of the exhibited microstructures in the ADI samples of Alloys A and B.

The analysis of the ADI microstructure shows that the austenitizing temperature has a meaningful influence on the number and size of the ferrite plates that are created during the subsequent process (i.e., austempering). Increases in the austenitizing temperature reduces the number of ferrite nuclei; therefore, the number of ferrite plates is lower, and the ferrite plates are thicker and longer. A smaller number of ferrite plates results in the creation of areas that are not involved in the austempering
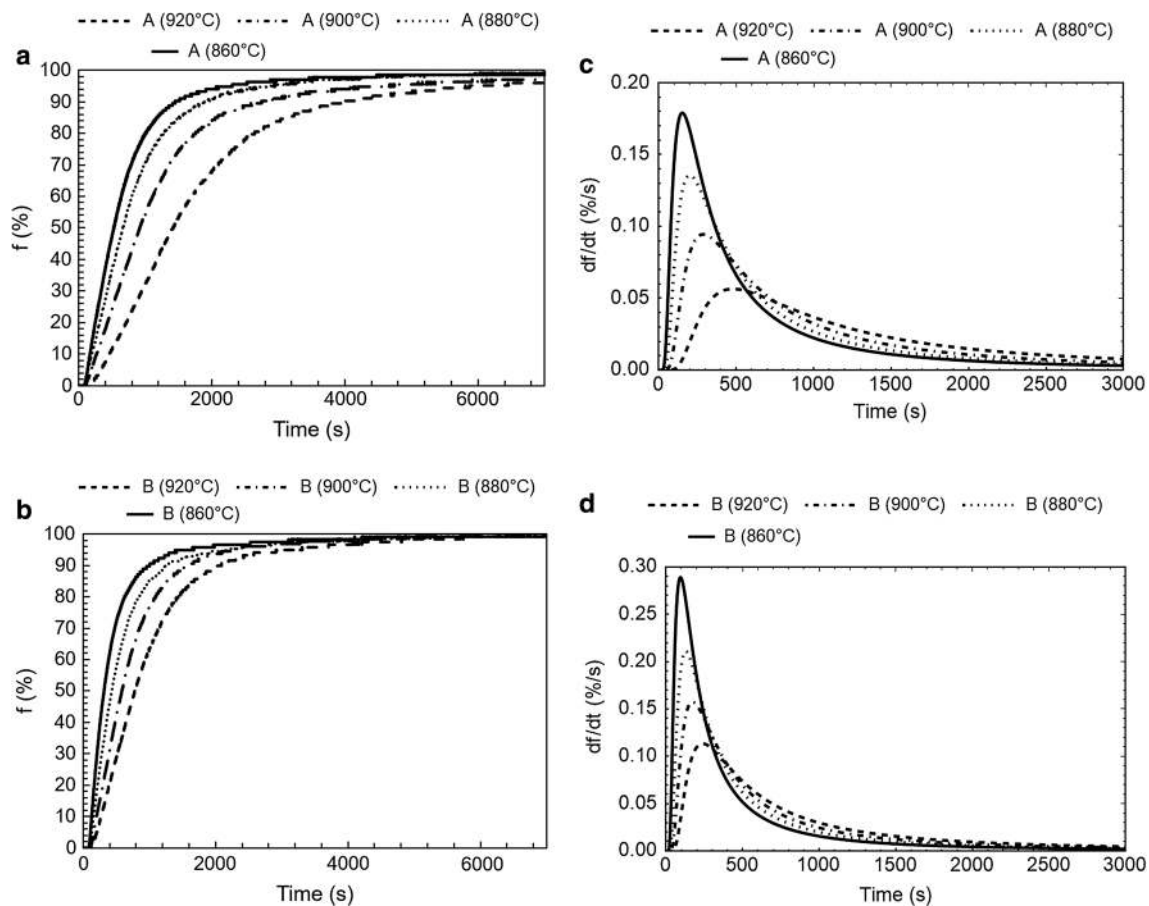
Fig. 4 Austempering transformation kinetics: **a**, **b**—transformed volume fractions; **c**, **d**—transformation rates

Table 2 Kinetic parameters for the austempering transformation

Alloy (temperature of austenitization)	Incubation time, t_{iA} (s)	Austempering transformation time (98% transformation), t_A (s)	Parameter n, $\times 10^3$ (Eq. 4)	Max. transition rate, df/dt (%/s)	Time for maximum. transition rate, t_{i-max} (s)
A (860 °C)	92	4475	3.30	0.18	168
A (880 °C)	88	4554	2.50	0.14	216
A (900 °C)	108	9210	1.74	0.09	291
A (920 °C)	175	10,425	1.04	0.06	480
B (860 °C)	90	3175	5.34	0.28	106
B (880 °C)	97	4057	3.89	0.21	137
B (900 °C)	114	3898	2.90	0.16	167
B (920 °C)	143	4813	2.09	0.11	243

transformation, which in turn may lead to the local inhomogeneity of the ausferrite. In extreme cases, this inhomogeneity may lead to the occurrence of martensite in these areas (Fig. 5d). Its presence was found in Alloy A for an austenitizing temperature of 920 °C. In Alloy B, no martensite was detected. The presence of martensite in Sample

A-920 °C is the result of a too-short time of austempering, which results from the dilatometer tests.

The results of the metallographic examinations in terms of the graphite nodules are summarized in Table 3.

In Alloy B, the number of graphite nodules is more than double that of Alloy A. This resulted in a decrease in the
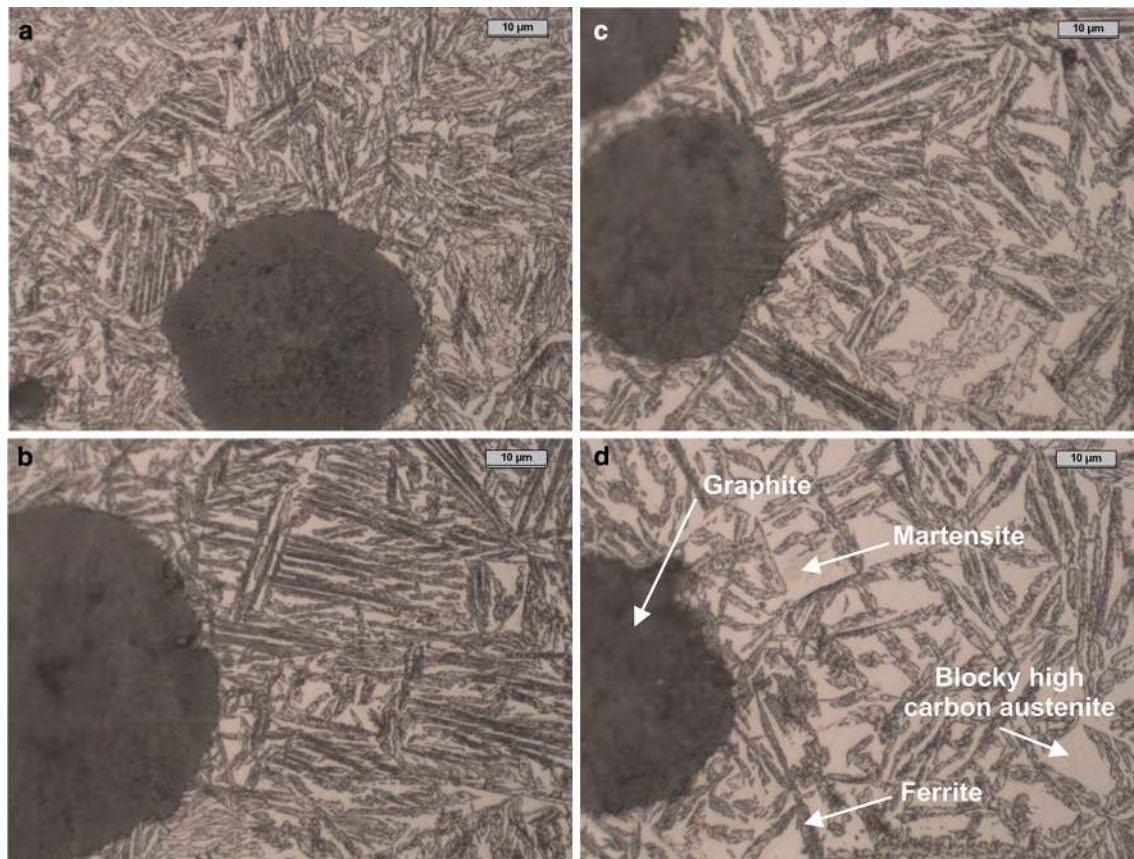
Fig. 5 Exhibited microstructures of ADI for investigated Alloy A: **a** austenitized at 860 °C; **b** austenitized at 880 °C; **c** austenitized at 900 °C; and **d** austenitized at 920 °C. Nital etched samples

mean free distance between the graphite nodules (by 36%). The great distances between the graphite nodules favor the inhomogeneity of the metallic matrix by the existence of areas of the blocky type of high-carbon austenite. These areas in particular are located at the boundaries of the eutectic grains, which are also promoted by the alloying elements that segregate to these regions (e.g., Mn, Mo).

The above analysis indicates that the homogeneity of the metallic matrix strongly depends on the austenitizing temperature and initial microstructure of the SGI. The number of graphite nodules plays an important role in the homogeneity of ausferrite. The data on thin-walled castings from SGI indicate that the number of graphite nodules in such castings can reach a few thousand per square millimeter [30]. Such a large number of graphite nodules significantly shortens the time of heat treatment, reduces the need for alloying additives, and decreases the heterogeneity of the metallic matrix.

The results of the austenite fraction calculations as a function of the austenitizing temperature are shown in Fig. 7.

From Fig. 7, it follows that the austenitizing temperature has a significant effect on the high-carbon austenite fraction. An increase in the austenitization temperature raises the austenite fraction in the microstructure. This is the result of a higher carbon content in the austenite with a rise in the austenitization temperature (as previously mentioned). The effect of increasing the austenite fraction is visible for Alloys A and B. The smaller increase in the austenite for Alloy B (as compared to Alloy A) is associated with the "refined" microstructure and higher number of ferrite nuclei formed at the beginning of the austempering transformation. In this connection, it can be stated that the coarser the initial microstructure of SGI, the more sensitive the castings are to the austenitizing temperature.

Fractures of the specimens (Alloy B) exhibit a mixture of ductile and cleavage fracture modes. Fracture (Fig. 8) revealed the presence of ellipsoidal-shaped precipitations from the Mg–Cu system identified as Mg_2Cu [28]. According to Zho [31], a thin Cu film on the spheroidal graphite surface is formed. In turn, an increase in the Mg content at the graphite-matrix interface occurs during the austenitizing of the SGI according to Dierickx [32]. This makes the possible reaction between Mg and Cu.

From the SEM observations, it follows that the density and size of the Mg_2Cu particles increase as the austenitizing temperature is raised. A scheme of the Mg–Cu particle creation is shown in Fig. 9.
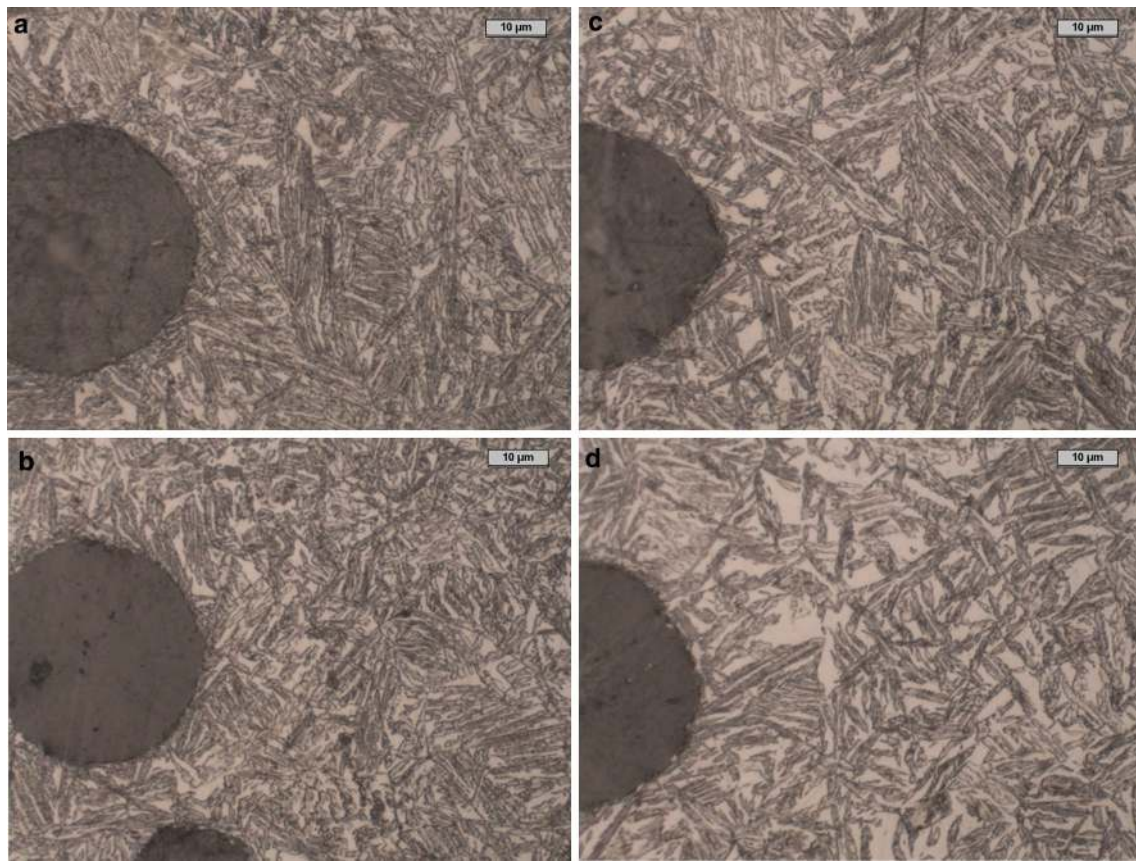
Fig. 6 Exhibited microstructures of ADI for investigated Alloy B: **a** austenitized at 860 °C; **b** austenitized at 880 °C; **c** austenitized at 900 °C; and **d** austenitized at 920 °C. Nital etched samples

Table 3 Results of metallographic examinations—graphite

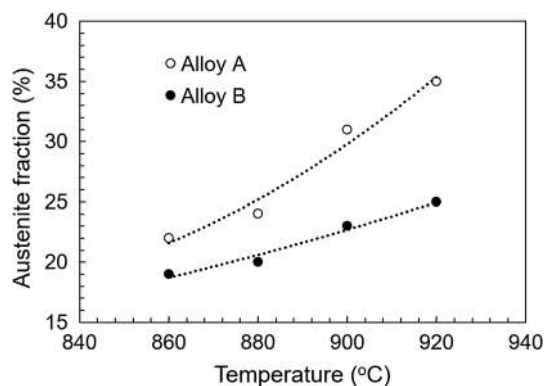| Alloy	Graphite fraction, g_f (%)	Number of graphite nodules, N_A (mm^{-2})	Mean free distance between graphite nodules, λ (µm)	Mean diameter of graphite nodules, d_{ek} (µm)
A	9.02	89	341	30.8
B	9.11	190	215	22.8

Fig. 7 Austenite fraction as function of austenitizing temperature

The mechanism of Mg–Cu precipitate formation (which is shown schematically in Fig. 9) consists of three stages:

1. The copper segregates negatively during crystallization, which means that the highest concentration is near the graphite nodules.
2. An increase in the Mg content at the graphite-matrix interface during austenitization (according to the work of Dierickx [32]).
3. The formation of Mg–Cu particles during the austenitizing process, which depends on the time and temperature of this heat treatment period.

From the experimental investigations, it can generally be stated that Mg–Cu particles occur throughout the entire austenitization temperature range tested. The higher the austenitizing temperature, the larger the observed Mg–Cu particles are. From [28], it follows that these highly dispersive Mg_2Cu particles present in the copper-alloyed ADI have a negative effect on the dynamic properties of the ADI.
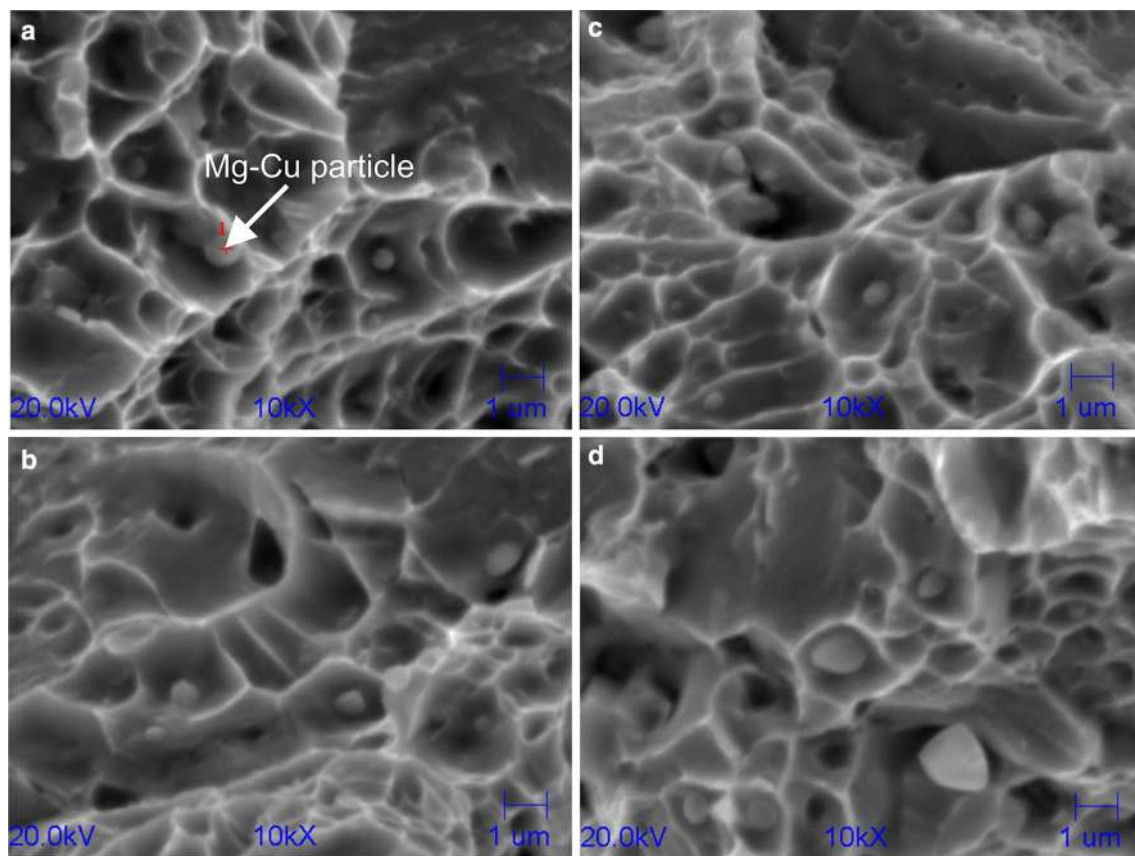
Fig. 8 Fracture after Charpy impact tests for Alloy B: **a** austenitized at 860 °C; **b** austenitized at 880 °C; **c** austenitized at 900 °C; and **d** austenitized at 920 °C
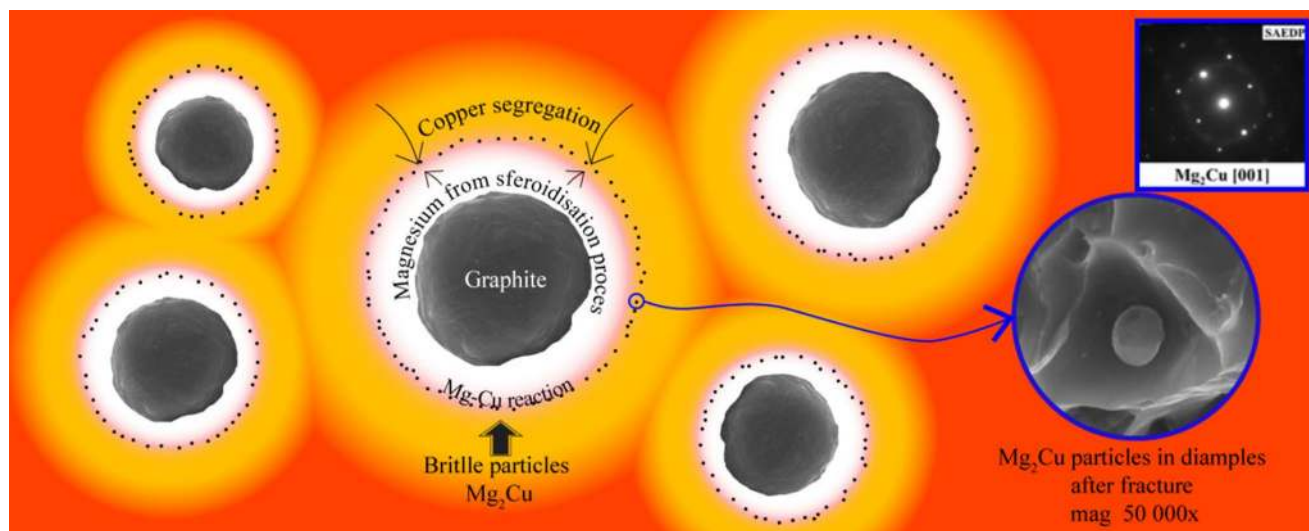

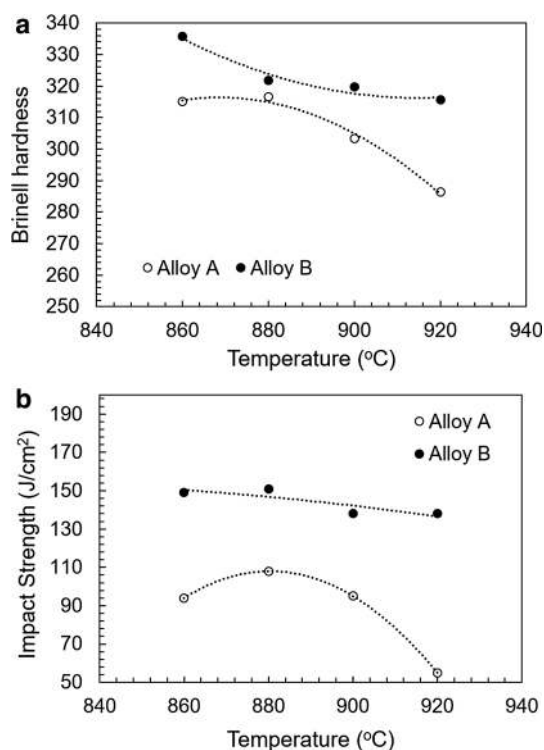**Fig. 9** Schematic of interaction between Mg and Cu during austenitization stage of ADI production

Fig. 10 Brinell hardness **a** and Charpy impact strength **b** as function of austenitizing temperature

3.4 Hardness and Charpy impact properties

Figure 10 shows the hardness as well as the impact properties for Alloys A and B with respect to the austenitizing temperature.

Figure 10a shows that the reduction of the austenitizing temperature increases the hardness of ADI cast iron. The higher austenite fraction contributed to reducing the hardness of the ADI cast iron. Figure 10a also shows that, at an austenitizing temperature of 880 °C, similar values were obtained for Alloys A and B. Increasing the number of ferrite plates and refining (change in morphology, number of ferrite plates) of the ausferrite contributes to the increased hardness of the ADI cast iron.

The impact tests have shown large differences in impact strength values for Alloys A and B (Fig. 10b). This is the result of the microstructure of the base SGI (degree of fineness of the graphite), which has a significant effect on the final impact strength of ADI castings. In the case of Alloy B, much higher impact values were attained as compared to Alloy A. As expected, the presence of martensite in the microstructure significantly reduced the impact properties of the ADI cast iron (for Alloy A austenitized at 920 °C). Figure 10b shows that, for Alloy B, the increase in the austenitizing temperature caused a slight reduction in the impact strength. The values of the impact strength for Alloy B are

much higher than for Alloy A. In addition, a reduction in impact strength (and hardness—Fig. 10a) was observed for Alloy B at an austenitizing temperature of 860 °C. The effect of reducing the impact strength and hardness at 860 °C can be caused by three phenomena. The first and most probable phenomenon is the greater segregation of the alloying elements. The low austenitizing temperature promotes greater heterogeneity in the austenite as a result of the slower diffusion processes. The second possible reason is the low carbon content in the austenite (see Eq. 3) as a result of the low austenitizing temperature. During the insufficient cooling rate from the austenitizing temperature to the range of austempering, a partial pearlitic transformation may occur due to the high diffusion rate of the carbon from austenite to graphite. Even the trace fraction of pearlite can significantly reduce the impact strength. The third reason may be the incomplete transformation of pearlite into austenite during the austenitization process. Then, pro-eutectoid ferrite occurs as a result of the low austenitizing temperature [33].

Increasing the fraction of austenite in ADI usually contributes to an increase in impact strength [11, 33–36]. Such a direction of interaction is related to the increase in austenite fraction due to the higher austempering temperature at a constant austenitizing temperature. The inverse effect of the austenite is observed when the increase in its fraction results from the increase in the austenitizing temperature; i.e., the reduction of the impact strength due to the increase in the fraction of the high-carbon austenite. This is also confirmed by Radulovic's study [37]. Thus, the austenitizing temperature plays an important role in the formation of a homogeneous structure that provides the optimal combination of mechanical properties (static and dynamic).

An important factor affecting the impact strength is also the presence of high-dispersive Mg–Cu particles. An increase in the austenitizing temperature contributes to the increase of the density and size of Mg–Cu particles (see Fig. 8), which has a negative effect on the impact strength. Therefore, the final impact strength is a result of the action of the austenite fraction and the presence of Mg–Cu particles.

4 Conclusions

The present study allows us to draw the following conclusions:

1. The austenitizing temperature has a significant effect on the transformation rate during the subsequent austempering process. Raising the austenitizing temperature reduces this transformation rate and also has a significant effect on the total transformation time, after which the microstructure of the ausferrite (irregular ferrite plates and stable high-carbon austenite) is achieved.

2. The austenitizing temperature plays an important role in the formation of a homogeneous structure. Raising the austenitizing temperature increases the austenite fraction, reduces the number of ferrite plates, and the ferrite plates are thicker and longer. A lower number of ferrite plates may lead to the local inhomogeneity of the ausferrite. In extreme cases, this inhomogeneity may cause the occurrence of martensite in these areas.

3. The mechanism of the formation of ellipsoidal-shaped Mg–Cu particles during the austenitizing process is presented. As the austenitizing temperature rises, the size and density of the Mg–Cu particles increases as well.

4. The austenitizing temperature has a very significant effect on mechanical properties. Increasing the austenitizing temperature decreases the structure homogeneity and the resultant hardness and impact strength of ADI.

References

1. M.M. Cisneros-Guerrer, R.E. Campos-Cambranis, M. Castro-Román, M.J. Pérez-López, Adv. Mater. Res. **4–5**, 415 (1997)
2. B.N. Olson, K.B. Moore, G.R. Simula, AFS Trans. **111**, 965 (2002)
3. O.E. Cekic, L. Sidjanin, D. Rajnovic, S. Balos, Met. Mater. Int. **20**, 1131 (2014)
4. N. Arab, J. Am. Sci. **7**, 49 (2011)
5. E. Nelson, Why ADI? Four applications where ADI is the material of choice and process considerations. *Ductile Iron Society 2016 World Conference on ADI*—October 27–28, 2016, pp. 1–6
6. M. Bamberger, *Encyclopedia of Iron, Steel, Their Alloy*, 5th edn. (Taylor and Francis, New York, 2016), pp. 196–216
7. Y. Tanaka, H. Kage, Mater. Trans., JIM **33**(6), 543 (1992)
8. A. Boccardo, M. Dardati, D.J. Celentano, L.A. Godoy, M. Gorny, E. Tyrała, Metall. Trans. B **47b**, 566 (2016)
9. A.D. Boccardoa, P.M. Dardatib, L.A. Godoya, D.J. Celentanod, Metall. Trans. B **49**(3), 1522 (2018)
10. W. Kapturkiewicz, E. Fraś, A.A. Burbelko, Mater. Sci. Eng., A **413–414**, 352 (2005)
11. B. Bosnjak, B. Radulovic, K. Pop-Tonev, V. Asanovic, J. Mater. Eng. Perform. **10**, 203 (2001)
12. N. Darwish, R. Elliott, Mater. Sci. Technol. **9**, 572 (1993)
13. N. Darwish, R. Elliott, Mater. Sci. Technol. **9**, 586 (1993)
14. N. Darwish, R. Elliott, Mater. Sci. Technol. **9**, 882 (1993)
15. R. Donnini, A. Fabrizi, F. Bonollo, F. Zanardi, G. Angella, Met. Mater. Int. **23**, 855 (2017)
16. E. Fraś, M. Górny, E. Tyrała, H.F. Lopez, Mater. Sci. Technol. **28**, 1391 (2012)
17. M. Górny, E. Tyrała, H.F. Lopez, J. Mater. Eng. Perform. **23**, 3505 (2014)
18. J. Mallia, M. Grech, Mater. Sci. Technol. **13**, 408 (1997)
19. N. Darwish, R. Elliott, Mater. Sci. Technol. **9**, 882 (1993)
20. K.L. Hayrynen, J. Keough, AFS Trans. **113**, 803 (2005)
21. S. Biswas, C. Monroe, T. Prucha, Int. J. Metalcast. **11**, 656–674 (2017)
22. F. Zanardi, Metall. Ital. **10**, 27 (2005)
23. A.P. Druschitz, D.C. Fitzgerald, *MADITM: Sae Technical Paper Series 2003-01-0831*, pp. 1–9
24. J.R. Keough, K.L. Hayrynen, G.L. Pioszak, AFS Trans. **10**, 1 (2010)
25. P.P. Rao, S.K. Putatunda, Mater. Sci. Eng., A **349**, 136 (2003)
26. K.B. Rundman, *The 35th Australian Foundry Institute National Conference* (Adelaide, Australian Foundary Institute, 2004)
27. D.J. Moore, T.N. Rouns, K.B. Rundman, AFS Trans. **94**, 255 (1986)
28. M. Górny, E. Tyrała, G. Sikora, Ł. Rogal, Met. Mater. Int. **24**(1), 96 (2018)
29. E. Tyrała, ISIJ Int. **54**, 700 (2014)
30. M. Górny, D.M. Stefanescu, in *Cast Iron Science and Technology ASM Handbook*, ed. by D.M. Stefanescu (ASM International, Ohio, 2017), p. 617
31. Y. Zou, M. Ogawa, H. Nakae, ISIJ Int. **52**, 505 (2012)
32. P. Dierickx, C. Verdu, A. Reynaud, R. Fougères, Scripta Mater. **34**, 261 (1996)
33. T.N. Rouns, K.B. Rundman, D.M. Moore, AFS Trans. **92**, 815 (1984)
34. Y.J. Kim, H.S. Hyounsoo, J.D. Lim, Mater. Lett. **62**, 357 (2008)
35. S.E. Kisakurek, A. Ozel, in *Ductile Iron Society, 2016 World Conference on ADI*—October 27–28, 2016
36. P. Sellamuthu, D.G. HarrisSamuel, D. Dinakaran, V.P. Premkumar, Z. Li, S. Seetharaman, Metals **8**, 53 (2018)
37. B. Radulovic, B. Bosnjak, R. Harding, K. Pop-Tonev, V. Asanovic, Mater. Tehnol. **28**, 307 (2004)